wind

MDPI

Article

On the Aerodynamic Characterisation and Modelling of Porous Screens for Building Applications

Marcello Catania *, Giulia Pomaranzi, Paolo Schito and Alberto Zasso

Department of Mechanical Engineering, Politecnico di Milano, via G. La Masa 34, 20156 Milano, Italy; giulia.pomaranzi@polimi.it (G.P.); paolo.schito@polimi.it (P.S.); alberto.zasso@polimi.it (A.Z.)
* Correspondence: marcello.catania@polimi.it

Abstract

The aerodynamic behaviour of buildings equipped with porous outer envelopes is governed by the interaction between millimetre-scale geometric features and building-scale flow structures. Explicitly resolving these scales in numerical simulations is computationally prohibitive, making homogenised porous-medium formulations a practical alternative. Among them, the Darcy–Forchheimer (D–F) model is widely adopted; however, the reliability of building-scale predictions critically depends on how its resistance coefficients are identified and validated. This study proposes and assesses a consistent procedure for the determination and application of D–F coefficients for porous screens used in double-skin façade systems. Porous elements are first characterised at the element scale through an analytical derivation based on aerodynamic force coefficients, from fully resolved CFD simulations of representative periodic modules. The resulting D–F coefficients are cross-compared and validated against available wind tunnel data at local Reynolds numbers $Re_H > 3000$. Secondly, the calibrated homogenised model is applied to a building-scale double-skin façade configuration. The porous layer is represented as a finite-thickness porous region governed by the identified D–F parameters and analysed through unsteady Reynolds-averaged Navier–Stokes simulations. The model's capability to reproduce global aerodynamic loads, local pressure distributions, and wake characteristics is evaluated against experimental data. The results demonstrate that a properly calibrated D–F formulation provides an accurate and computationally efficient representation of porous façade systems, bridging element-scale characterisation and structural-scale aerodynamic performance.

Keywords: permeable double skin façades; porous screens; porosity; CFD; Darcy–Forchheimer

Academic Editor: Xiaolei Yang

Received: 30 March 2026
Revised: 22 April 2026
Accepted: 29 April 2026
Published: 9 May 2026

1. Introduction

Porous envelopes such as perforated panels, expanded meshes, and louvres are increasingly adopted in civil engineering as passive devices to mitigate wind effects. In buildings, these elements are frequently integrated as outer skins, leading to permeable double-skin façade (PDSF) systems. By allowing partial airflow through the external layer, these systems modify the pressure distribution around the structure and alter wake development, influencing both global wind loads and local aerodynamic phenomena [1–4].

From a fluid-mechanics perspective, the aerodynamic behaviour of structures equipped with porous envelopes constitutes a multi-scale problem. The characteristic dimensions of the porous elements are typically on the order of centimetres, whereas the building scale is measured in tens of metres. Directly resolving the porous geometry in

Computational Fluid Dynamics (CFD) requires capturing a wide range of spatial and turbulence scales, leading to prohibitive computational costs and severe mesh constraints [5–7]. At the same time, recent experimental and high-fidelity numerical studies have highlighted the strong sensitivity of the aerodynamic response to small-scale geometric features, further emphasising the intrinsic multi-scale nature of the problem [8,9].

A viable alternative consists of adopting homogenised porous-medium models, in which the detailed geometry is not explicitly resolved, and its macroscopic aerodynamic effect is represented through additional momentum sink terms. Among the available formulations, different approaches have been proposed, each characterised by specific advantages and limitations. Pressure-jump models represent the porous layer as a discontinuity with a prescribed resistance [10,11]. While computationally efficient, they may suffer from numerical instability for low-porosity media and are inherently limited in representing tangential momentum exchange [12,13]. To overcome these limitations, pressure–velocity jump formulations have been introduced to account for both normal and shear stresses, improving the representation of skewed-flow conditions and complex flow orientations [13,14].

Alternatively, the Darcy–Forchheimer (D–F) model distributes viscous and inertial pressure losses across a finite porous thickness [15,16], providing a more physically consistent representation of momentum dissipation within the porous layer, and generally improving numerical robustness compared to localised pressure-jump approaches, particularly for low-porosity media [12]. In high-Reynolds-number flows typical of wind engineering applications, the inertial (Forchheimer) contribution dominates, allowing simplified parameterisations [17,18]. The porous medium is commonly represented through diagonal components of a resistance tensor [19], although more complex geometries such as louvres or expanded meshes may require a full matrix representation to capture anisotropic effects [20,21]. Despite its widespread use, the predictive capability of the D–F formulation strongly depends on the definition of its resistance coefficients and on the assumptions adopted for their derivation.

The primary advantage of homogenised methods lies in their ability to reproduce the global aerodynamic effect of complex porous geometries using a limited set of coefficients. These coefficients can be derived experimentally [9], through semi-empirical correlations [8], or via fully resolved numerical simulations [18]. Nevertheless, their definition remains one of the main sources of uncertainty. Experimental approaches are often configuration-specific, while semi-empirical correlations may not generalise across different geometries and flow regimes. Even when derived from high-fidelity numerical simulations, the resulting parameters are rarely validated outside the calibration setup. Recent studies on the interaction between porous layers and solid obstacles further highlight the challenges associated with model transferability in realistic configurations [22].

Despite the increasing adoption of porous-medium models in building aerodynamics and other wind engineering applications [4,13,23,24], two fundamental limitations can be identified in the current literature:

1. A lack of consistent methodologies to derive model coefficients directly from the geometrical properties of the porous medium, ensuring physical interpretability and robustness;
2. A limited validation of homogenised approaches when applied to realistic building-scale configurations, where complex flow interactions may alter their predictive capability.

Existing studies typically address these aspects separately, focusing either on coefficient identification at the element scale or on large-scale applications assuming predefined parameters. A comprehensive and validated framework linking geometrical characterisation, coefficient identification, and structural-scale aerodynamic response is still lacking.

The main contribution of this work is therefore twofold: (i) the definition of a practical and consistent procedure to determine Darcy–Forchheimer coefficients directly from the geometrical properties of porous screens and (ii) the verification of the accuracy and transferability of the homogenised model when applied to a building-scale double-skin façade configuration. By addressing both coefficient identification and large-scale validation within a unified framework, this study aims to contribute toward the development of reliable predictive methodologies for porous envelopes in wind engineering applications.

2. Methodology

The methodological framework adopted in this study is structured in two consecutive parts. The first part addresses the aerodynamic characterisation of porous screens and the identification of the corresponding D–F coefficients. The second part evaluates the validity and transferability of the identified coefficients when applied to a building-scale double-skin façade configuration. The overall workflow moves from element-scale characterisation to building-scale application.

2.1. Porosity Characterisation and Identification of D–F Coefficients

The objective of the first part is to establish a consistent procedure for deriving homogenised D–F coefficients starting from the geometrical description of a porous screen. In this stage, a planar porous configuration is considered, as shown in Figure 1. The selected geometry consists of a perforated panel with a thickness of 2 mm and square openings with hydraulic diameter $D_H = \frac{4A_H}{P} = 29.5$ mm (with P the perimeter of an individual hole and A_H its area), resulting in a porosity (ratio of open to total area) equal to 65.8%. This pattern is adopted as a representative case of planar permeable screens, as highlighted by [25], who demonstrated similar aerodynamic behaviour across planar configurations with different geometries.

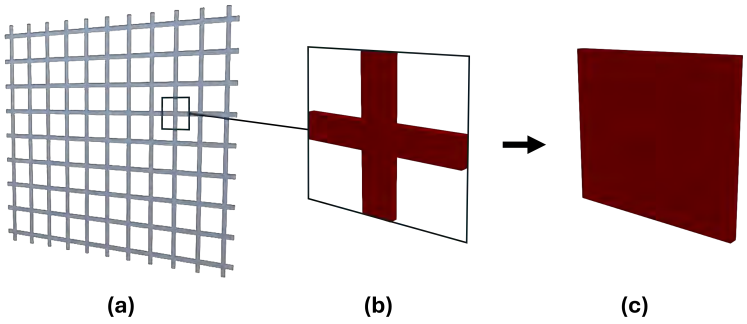

Figure 1. From left to right: (**a**) experimental grid, (**b**) explicit representation of a periodic unit cell for the modulus simulation, (**c**) equivalent homogenized porous medium for the modulus simulation.

The identification process follows a three-step workflow:

1. Fully resolved CFD simulations are performed on representative periodic modules of the porous geometry to provide reference data. In this "modulus approach", the actual perforation pattern is explicitly modelled within a computational domain designed to reproduce uniform inflow conditions. To capture the screen's directional sensitivity, the inflow angle α is systematically varied from 0° to 90° in the x-y plane by imposing an inlet velocity vector $[U\cos\alpha, U\sin\alpha, 0]$. A dataset of integrated aerodynamic forces $[F_x(\alpha), F_y(\alpha), F_z(\alpha)]$ is thus generated.
   Given the double symmetry of the perforated mesh under investigation, the resistance tensor is diagonal, and no variation in the x-z plane is necessary as the aerodynamic behaviour in that plane is assumed to be identical to the x-y plane.

It is worth noting that this assumption is not a general limitation of the proposed methodology but rather a consequence of the symmetry properties of the specific porous geometry considered. The identification procedure itself is not restricted to diagonal tensors, as it is based on fitting force–velocity relationships obtained at multiple flow orientations. In this sense, the approach can be directly extended to anisotropic porous media requiring a full tensorial representation, including off-diagonal terms. The present work focuses on a planar perforated configuration for which diagonal dominance is physically justified and supported by the results.

2. The force–velocity relationship obtained from the simulations is then mapped into the analytical model developed by Marykovskiy et al. [18] that links the Darcy–Forchheimer tensorial formulation with the measured physical quantities. The analytical formulation is briefly described in Appendix A.
3. A least-squares algorithm is then employed to minimise the residuals between the forces obtained from the resolved CFD simulations and the predictions derived from the analytical solution. The process identifies the optimal tensor components that provide the best fit across the tested angles. The obtained results are then validated against wind tunnel experimental data.

2.2. Application to Building Aerodynamics

In the second part of the study, the calibrated D–F model is applied to a building-scale configuration in which a porous screen acts as an outer layer of a double-skin façade system. In this context, the porous geometry is no longer resolved explicitly; instead, it is represented as a finite-thickness porous region governed by the homogenised D–F formulation derived in the first part.

A computational model of the building is developed to reproduce the relevant aerodynamic features of the installation context. The governing Navier–Stokes equations are modified to include momentum sink terms according to the D–F model within the porous region. Unsteady Reynolds-Averaged Navier–Stokes (URANS) simulations are performed to capture both mean and unsteady flow characteristics while maintaining computational efficiency at the structural scale.

The underlying assumption relies on scale separation: the interaction between the flow and the porous medium occurs at the pore scale, whereas building-scale disturbances (e.g., separation, recirculation, and downwash) act at much larger scales. The porous-medium effect is modelled through the D–F coefficients, while the larger-scale flow structures are directly resolved by the CFD simulation. In this framework, the coefficients identified at the element scale are expected to retain their predictive capability when applied to building-scale configurations, where the incoming flow may be significantly perturbed.

Given that the primary objective is to assess the capability of the D–F model to reproduce the aerodynamic behaviour of porous double-skin façades, a sectional two-dimensional (2D) configuration is adopted. This modelling choice allows isolation of the fundamental flow–structure interaction mechanisms by excluding end effects and focusing on the coupling between the porous layer and the solid building core.

The assessment focuses on multiple levels of aerodynamic response. At the global level, overall force coefficients and related integral quantities are evaluated to determine the effect of the porous layer on the building's wind loading. At the local level, pressure coefficient distributions on both the porous screen and the underlying solid façade are analysed to quantify pressure redistribution within the cavity and across the envelope. Finally, wake properties are investigated through analysis of velocity fields, vortex shedding behaviour, and characteristic frequencies, allowing verification of the model's capability to reproduce unsteady aerodynamic phenomena.

The results obtained with the homogenised porous model are compared with experimental data from wind tunnel tests, where the building model is equipped with the permeable façade. This comparison enables assessment of the transferability of the identified D–F coefficients from simplified element-scale conditions to complex building-scale flow environments. Particular emphasis is placed on evaluating whether the homogenised approach can simultaneously reproduce global loads, local pressure effects, and wake dynamics without explicit resolution of the porous geometry.

It should be noted that the present validation is limited to a simplified sectional configuration and specific flow conditions. While the results demonstrate the robustness of the proposed approach, further investigations on fully three-dimensional configurations are required to assess the general applicability of the methodology under more complex flow scenarios.

The paper is structured as follows: in the Section 3, the experimental tests used for validation purposes are introduced. Afterwards, Section 4 describes the numerical setup employed for porosity characterization, the "modulus configuration" (Section 4.1), and the application to building aerodynamics, the "sectional simulation " (Section 4.2). Results are presented and discussed in order in Section 5 and conclusions are drawn in Section 6.

3. Experimental Setup

As previously anticipated, the results of the building-scale simulations are validated against experimental data; therefore, this section briefly describes the wind tunnel setup and test conditions adopted as a reference.

The experimental benchmark for this study is derived from a wind tunnel campaign aimed at characterising the aerodynamic response of a square prism under different envelope conditions. The physical model consists of a rigid square prism with a side length $D = 0.2$ m and an aspect ratio $H/D = 6$, representative of a typical high-rise building configuration (Figure 2). To capture the spatial and temporal variations of the surface pressure field, the model is equipped with 128 pressure taps distributed across four different levels.

For the validation of the 2D CFD sectional model, pressure data from the middle floor (Level 2, located at $z = 0.65H$) is selected. This choice is intended to minimise the influence of three-dimensional end effects, such as the downwash from the free end and the upwash from the floor, which are known to alter wake coherence and the vortex-shedding mechanism [26,27].

Two distinct façade configurations are implemented on the same model:

- *Naked configuration*: Simulating a standard single-glazed cladding system (Figure 2a).
- *Porous configuration*: Replicating a permeable double-skin façade (PDSF) by integrating a perforated mesh (Figure 2b). The shroud, described in Section 2.1 is positioned at a distance $d = 0.125D$ from the primary solid façade.

All tests are conducted in the atmospheric boundary layer section of the Politecnico di Milano Wind Tunnel (GVPM) under smooth flow conditions (turbulence intensity $I_u \approx 2\%$, integral length scale $L_u^x = 0.2$ m measured 1 m from the ground). Measurements are repeated at multiple flow velocities ($U = 5, 8,$ and 10 m/s) to ensure Reynolds independence and verify the repeatability of the results. The reference velocity is monitored using a Pitot tube positioned $35D$ upstream of the model at a height of $z = 5D$ from the wind tunnel floor.

The aerodynamic quantities extracted from the experimental data and subsequently used for CFD validation include

- Global force coefficients: the instantaneous drag and lift coefficients are calculated as

$$C_F(t) = \frac{F(t)}{0.5\rho U^2 Bh} \tag{1}$$

where $F(t)$ is the aerodynamic force obtained by integrating the surface pressures on Level 2, $B = D$ is the characteristic dimension, and $h = 1.2D$ is the tributary height of the considered level.

- Strouhal number: the non-dimensional vortex-shedding frequency is defined as

$$St = \frac{f_{vs} D}{U} \tag{2}$$

where f_{vs} is identified as the dominant peak in the power spectral density (PSD) of the cross-wind force.

- Local pressure coefficient: the surface pressure distribution is evaluated as

$$C_p(t) = \frac{p(t) - p_{ref}}{0.5\rho U^2} \tag{3}$$

where $p(t)$ is the instantaneous pressure at the tap location and p_{ref} is the static reference pressure.

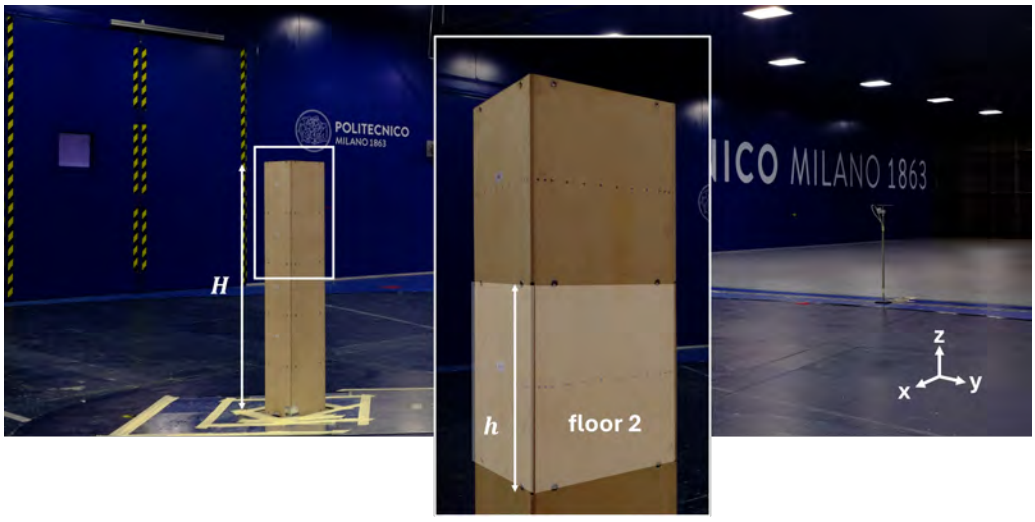

(**a**)

(**b**)

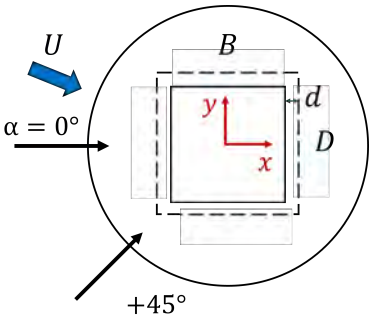

(**c**)

Figure 2. Experimental wind tunnel setup: (**a**) overview of the rigid square prism in the naked configuration; (**b**) detail of the prism equipped with the porous envelope, where the dashed frame highlights the region of the permeable screen; (**c**) schematic of the reference system and definition of the wind angles of attack.

4. Numerical Setup

All the numerical simulations are performed using the open-source CFD software OpenFOAM v2112, which utilizes a finite-volume method for the spatial discretization of the governing equations [28]. The flow is treated as incompressible, and the turbulence closure is achieved through the URANS equations. The k-ω SST (Shear Stress Transport) model is selected to describe the turbulent viscosity.

This modelling approach is chosen to balance predictive accuracy with computational efficiency, representing a well-established standard for the aerodynamic characterization of porous media [11,22,25] and for investigating fluid–structure interaction (FSIs) in sectional models [6,7,29,30]. In the following sections, the specific numerical setups for both the modulus-scale and the building-slice simulations are detailed, alongside the experimental wind tunnel benchmarks used for validation.

4.1. Modulus Simulations

For the aerodynamic characterization of the porous medium, steady-state RANS simulations are employed. Since the study focuses on the estimation of time-averaged aerodynamic loads, the RANS approach represents the standard and most practical choice in accordance with established porous media literature [11,22,25].

The solver employed is `simpleFoam`, utilising the standard SIMPLE pressure–velocity coupling algorithm. Convective terms are discretised using second-order upwind schemes, while diffusive terms adopt central differencing. Gradients are linearly interpolated, and turbulence quantities rely on wall functions for k, ω, and turbulent viscosity ν_t. Adaptive low-Re wall functions available in OpenFOAM (e.g., *kqRWallFunction* and *omegaWallFunction*) are selected to ensure physical consistency at all y^+ values [31], allowing the model to correctly resolve the boundary layer regardless of local mesh refinement. Convergence is enforced by monitoring both residual decay, required to fall below 10^{-6} for momentum and 10^{-7} for turbulence variables, and the stability of the integral forces monitored on the plate.

The modulus domain represents the elementary periodic unit cell of the perforated element. By defining all lateral faces as cyclic boundary conditions, the model simulates an infinitely periodic plate, effectively isolating the intrinsic aerodynamic properties of the medium from edge- or frame-induced disturbances. The objective is to characterise the drag and lift action on the plate at different angles of attack (α); thus, the inlet velocity vector has been defined via its projected components. For the analysis of skew inflow, angles of attack from 0° to 90° with a 10° step have been tested. The inlet velocity components are prescribed as

$$u_x = U\cos\alpha, \qquad u_y = U\sin\alpha, \tag{4}$$

where the secondary direction corresponds to the in-plane periodic direction of the modulus. The imposed boundary conditions are detailed in Table 1. To summarise, a fixed static pressure is prescribed at the outlet, lateral faces are defined as cyclic, and the plate surfaces are treated as no-slip walls with appropriate wall functions. Simulations are repeated at three streamwise velocities (4.5 and 10 m/s) to verify the Re-independency of the results. As observed by Allori et al. [32], the governing parameter is the local Reynolds number $Re_H = \frac{\rho U D_H}{\mu} > 3000$, which ensures results stability.

The modulus has a constant thickness $t = 2$ mm and a gross area $A = b_H \times h_H = 33.7$ mm $\times$ 38.8 mm, consistent with the experimental samples. The domain upwind and downwind dimensions are chosen as $10D_H$ and $20D_H$ (Figure 3a) as a result of a sensitivity study, in accordance with similar literature investigations [25].

In the implicit simulation, the explicit plate geometry (Figure 3b) is substituted with a homogeneous set of cells of the same dimensions (Figure 3c). Within this zone, the Darcy–

Forchheimer porosity treatment is active, utilising coefficients derived from the explicit simulations. Further details are reported in Section 4.3. To ensure a consistent comparison, the mesh properties are kept constant between the two modelling approaches.

For all simulations, the integrated forces on the perforated surface or the porous slab are extracted to calculate the drag and lift coefficients. In the following sections, results are discussed using C_D as the primary aerodynamic load descriptor.

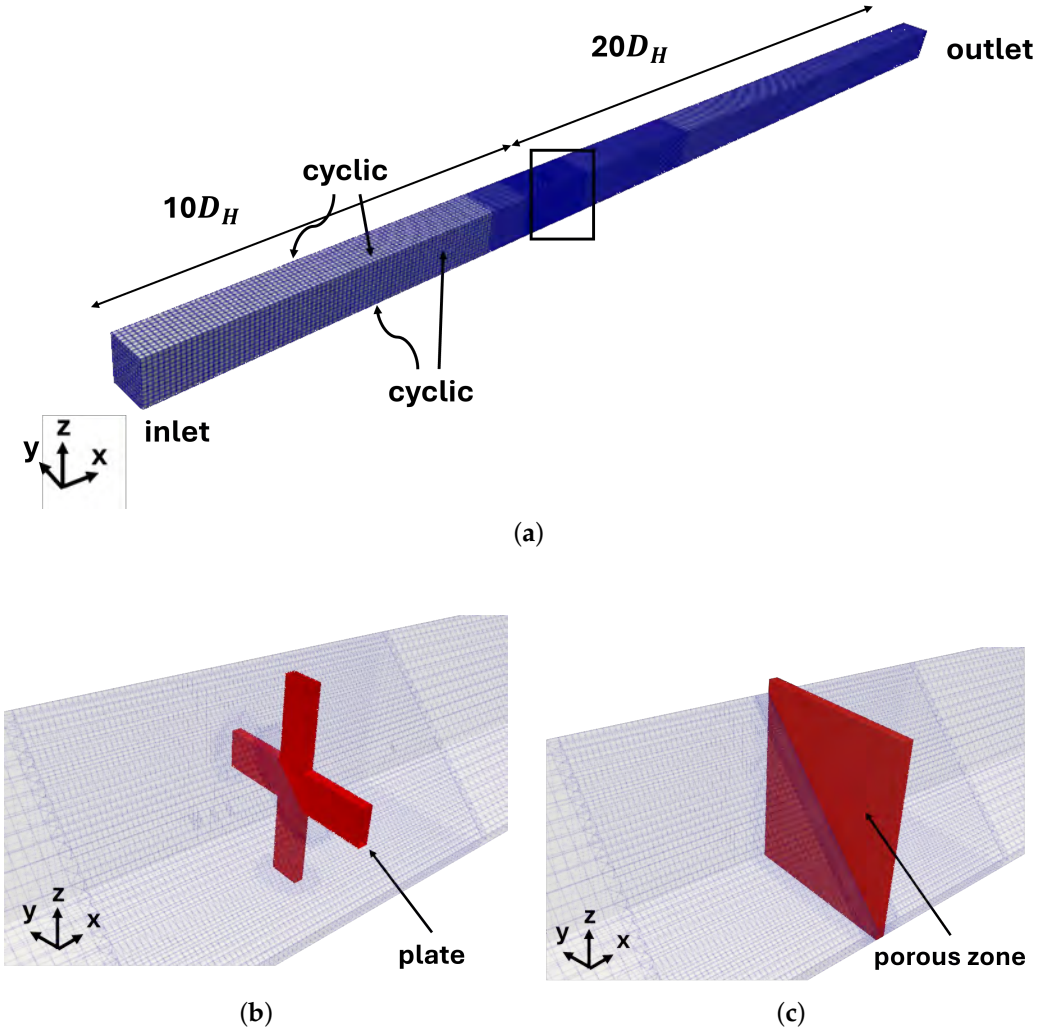

Figure 3. Modulus configuration, numerical domain overview with geometric dimensions: (**a**) overview of the periodic unit cell domain and boundary conditions; (**b**) detail of the explicitly resolved perforated geometry; (**c**) detail of the homogenized porous region used in the implicit modeling approach.

Table 1. Boundary conditions (BCs) for cyclic domains. The patch names are indicated in the columns, while each row addresses the specific BC employed.

Field	Inlet	Outlet	Lateral	Plate
p	zeroGradient	fixedValue (0)	cyclic	zeroGradient
U	fixedValue (U)	inletOutlet	cyclic	noSlip
ν_t	calculated	calculated	cyclic	nutkWallFunction
k	fixedValue	inletOutlet	cyclic	kqRWallFunction
ω	inletOutlet	inletOutlet	cyclic	omegaWallFunction

Modulus Simulations — Mesh Generation and Independence Study

The mesh is generated with `blockMesh` and `snappyHexMesh`, following a consistent refinement strategy. Coarser background regions are combined with progressively refined boxes around the plate. The final mesh is characterised by a total of 290,000 cells, with a minimum cell size l_{min} of approximately 0.42 mm near the perforation edges (Figure 3b). This small element size grants an adequate resolution of the geometry (see Table 2, $\frac{H}{l_{min}}$ metric) and a maximum y^+_{max} lower than 10.

A mesh-independence analysis is performed by repeating selected simulations on systematically refined grids to ensure numerical convergence. Table 2 presents the drag coefficients C_D at zero attach angle $\alpha = 0°$. Three mesh resolutions, coarse, standard, and fine, are compared. The aerodynamic loads showed negligible variations (below 1%) between the standard and fine refinements, indicating that the adopted resolution is sufficient to provide mesh-independent results for all investigated geometries.

Table 2. Comparison of the drag coefficient C_D at zero attach angle $\alpha = 0°$ for the adopted mesh, a coarser and a finer version, modulus configuration. $U = 5\,\mathrm{m/s}$.

Mesh	$N_{cells}/10^3$ [−]	H/l_{min} [−]	y^+_{max} [−]	C_D [−]
Coarse	100	27	29	1.60
Adopted	290	80	9.4	1.54
Fine	350	96	7.8	1.55

4.2. Sectional Simulations

The second phase of the investigation analyses the aerodynamic behaviour of a square cylinder ($B/D = 1$) equipped with a porous envelope through 2D URANS simulations. The study focuses on both global and local aerodynamics, evaluating the total lift and drag coefficients, vortex-shedding characteristics, and the pressure distribution on the façades once a statistically steady-state regime is reached.

In this study, a 2D approach is adopted, implying that an infinite sectional model of the prism is considered. Under this condition, the flow is assumed to be fully correlated along the spanwise direction. This simplification offers two primary advantages: (i) it significantly reduces the computational cost by reducing the cell count, thereby enabling an extensive parametric investigation across multiple configurations, and (ii) it allows for the isolation of porosity-induced effects by eliminating the influence of end-effects and other complex finite-geometry phenomena. This approach is consistent with established practices in wind engineering, where sectional 2D simulations are commonly employed to investigate fundamental flow mechanisms and provide benchmark comparisons for bluff-body aerodynamics.

Admittedly, validating a 2D numerical model against 3D experimental data from wind tunnel (WT) tests presents challenges, as end-effects such as tip-vortices and downwash can significantly modify both local and global aerodynamic quantities [26,27]. However, this approach is justified by the current scarcity of literature data on porous-shrouded structures suitable for validation and the necessity of establishing a fundamental, reproducible numerical benchmark. To mitigate the discrepancies between the 2D and 3D setups, experimental data from Floor 2 (middle level) of the model are selected as the reference for validation. This section is located sufficiently far from the free-end and the floor to approximate the two-dimensional flow behaviour characterised by higher spanwise coherence.

The computational domain extends $150D$ in the streamwise direction and $100D$ in the cross-wind direction, as illustrated in Figure 4a. This expansive domain ensures a negligible blockage ratio and prevents boundary interference with the wake development, regardless of the angle of attack. At the inlet, a constant velocity U is prescribed with a zero-gradient

pressure condition, while a fixed atmospheric pressure is set at the outlet. The upper and lower boundaries utilise symmetry conditions to simulate undisturbed free-stream flow, consistent with established practices for vortex-shedding studies on fixed prisms [7,33,34].

To reproduce skewed wind conditions, the inlet velocity components are defined as Equation (4).

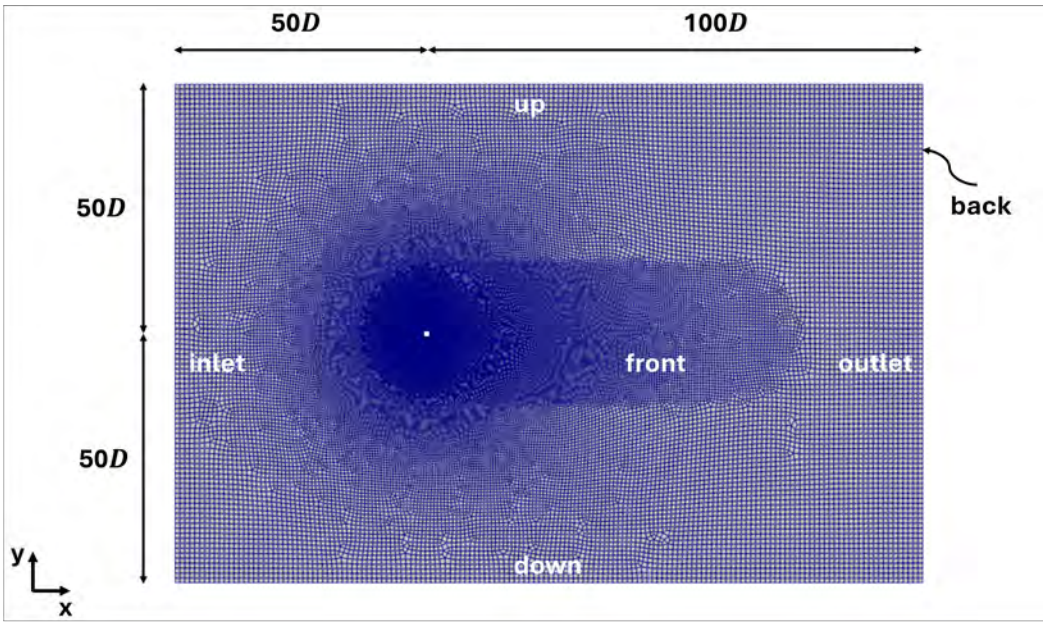

(**a**)

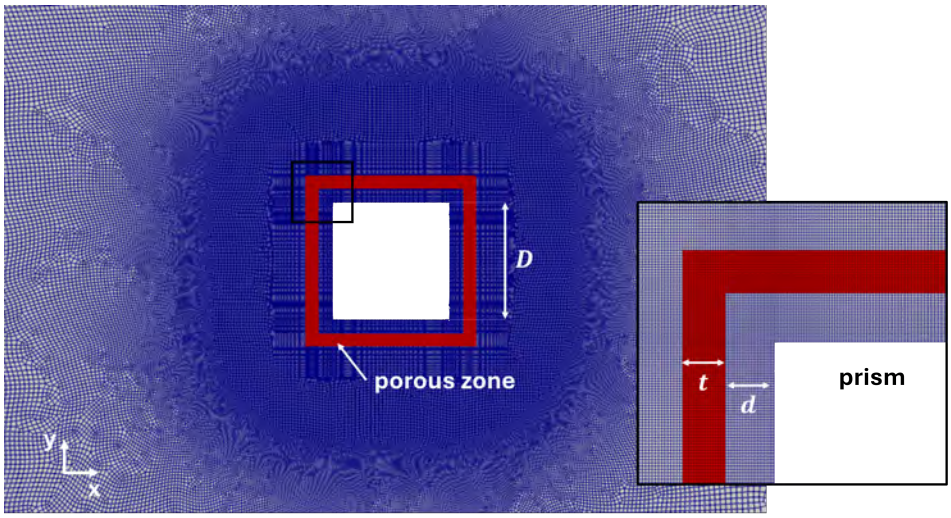

(**b**)

Figure 4. 2D slice configuration, numerical domain overview with geometric dimensions: (**a**) overview of the full computational domain and boundary conditions; (**b**) detail of the mesh refinement around the square prism and the porous envelope region.

The cylinder walls are modelled with no-slip conditions, utilizing adaptive low-Reynolds wall functions to maintain boundary layer consistency across the y^+ range. The boundary conditions are summarised in Tables 3 and 4.

To simulate the porous envelope, a special set of cells of thickness $t = 0.1D$ is placed at $d = 0.125D$ around the prism (see detail in Figure 4b), mimicking the experimental setup. Within this zone, the Darcy–Forchheimer porosity treatment is active, employing

the coefficients derived from the modulus simulations. Further details are reported in Section 4.3.

Table 3. Boundary conditions for the sectional simulations.

Field	Inlet	Outlet	Top/Bottom	Cylinder Walls
p	zeroGradient	fixedValue (0)	symmetry	zeroGradient
U	fixedValue (U)	inletOutlet	symmetry	noSlip
k, ω, ν_t	fixedValue	inletOutlet	symmetry	Wall Functions

High-fidelity spatial and temporal discretisation is ensured via second-order numerical schemes. Time integration employs the Crank–Nicolson scheme. For cell-to-face interpolations, linear schemes are used, while gradient terms are discretised using a cell-limited Gauss scheme to ensure boundedness. Divergence terms are handled via Gauss linear schemes, and Laplacian terms utilize Gauss linear interpolation with a limited surface-normal gradient for non-orthogonal corrections. An adaptive time step is used to maintain a maximum Courant number of 0.6. Aerodynamic metrics are calculated over at least 10 vortex-shedding cycles after the initial transient phase has been discarded.

Table 4. Boundary conditions for 2D slice domain. The patch names are indicated in the columns, while each row addresses the specific BC employed.

Field	Inlet	Outlet	Up/Down	Front/Back	Prism
p	zeroGradient	fixedValue (0)	freestreamPressure	empty	zeroGradient
U	fixedValue (U)	inletOutlet	freestream	empty	noSlip
ν_t	calculated	calculated	calculated	empty	nutkWallFunction
k	fixedValue	inletOutlet	freestream	empty	kqRWallFunction
ω	inletOutlet	inletOutlet	freestream	empty	omegaWallFunction

Sectional Simulations — Mesh Generation and Independence Study

The computational mesh, illustrated in Figure 4, consists of approximately 154,000 predominantly hexahedral cells, designed to provide high-resolution mapping of the velocity field within the domain. The grid is generated using the open-source utility `Gmsh`. Given the 2D nature of the simulation, the domain is defined with a single cell thickness in the spanwise (z) direction.

A progressive refinement strategy is implemented, transitioning from a background cell size of D in the far-field to a minimum resolution of $0.015D$ at the prism walls. This refinement ensures a maximum dimensionless wall distance $y^+_{max} \approx 50$ for the considered Reynolds numbers. Since shear layer separation and the resulting vortex dynamics are critically sensitive to edge sharpness and local gradients [35–37], specific care is devoted to the mesh topology near the trailing and leading edges, as highlighted in the detailed view in Figure 4b.

To ensure the numerical solution is independent of the spatial discretisation, a mesh independence study is conducted by systematically varying both the background cell dimensions and the refinement levels near the prism. The performance of the selected mesh is benchmarked against a finer grid configuration. The comparative results, summarised in Table 5, focus on the primary aerodynamic metrics: the Strouhal number (St), the mean drag coefficient ($C_{D,m}$), and the standard deviation of the lift coefficient ($std(C_L)$). The study indicates that the variations in these integral quantities are lower than 1%, confirming that the adopted mesh provides a sufficient balance between computational economy and numerical accuracy.

Table 5. Comparison of the mean drag coefficient $C_{D,m}$, standard deviation of the lift coefficient $std(C_L)$ and Strouhal number St for the adopted mesh, a coarser and a finer version, 2D slice configuration, $\alpha = 0°$, $U = 5$ m/s.

Mesh	$N_{cells}/10^3$ [−]	D/l_{min} [−]	y^+_{max} [−]	St [−]	$C_{D,m}$ [−]	$std(C_L)$ [−]
Coarse	80	67	50	0.114	1.99	1.31
Adopted	154	67	50	0.123	2.05	1.48
Fine	240	134	15	0.120	2.03	1.41
Very fine	500	134	15	0.121	2.05	1.40

4.3. Porous Medium Modelling

In both the implicit modulus configurations (Figure 3c) and the 2D building-scale simulations (Figure 4b), the porous envelope is modelled as a homogenised medium using the D–F approach. The porous layer is represented as a region of finite thickness t, where a momentum sink term $\mathbf{S_p}$ is added to the Navier–Stokes equations to account for the flow resistance. According to the Darcy–Forchheimer law, this sink term is defined as

$$\mathbf{S_p} = -\left(\mu \mathbf{D}\mathbf{u} + \frac{1}{2}\rho|\mathbf{u}|\mathbf{F}\mathbf{u}\right) \tag{5}$$

where $\mathbf{u}$ is the local velocity vector; $|\mathbf{u}|$ is its magnitude; μ and ρ are the fluid dynamic viscosity and density, respectively; and $\mathbf{D}$ and $\mathbf{F}$ are the Darcy (viscous) and Forchheimer (inertial) resistance tensors.

In wind engineering applications involving high-Reynolds-number flows through perforated screens or ouvres, pressure-driven inertial losses significantly outweigh viscous stresses [18,24,25]. Consequently, the Darcy term ($\mathbf{D}$) can be neglected. This approximation is applied only in the identification of the porous-medium coefficients. In the building-scale simulations, the full viscous contribution is retained in the governing equations. The modified momentum equation for incompressible flow thus becomes

$$\rho\left(\frac{\partial u_i}{\partial t} + u_j\frac{\partial u_i}{\partial x_j}\right) = -\frac{\partial p}{\partial x_i} + \mu\frac{\partial^2 u_i}{\partial x_j \partial x_j} - \frac{1}{2}\rho|\mathbf{u}|f_{ij}u_j \tag{6}$$

where f_{ij} represents the components of the Forchheimer resistance tensor $\mathbf{F}$:

$$\mathbf{F} = \begin{bmatrix} f_{xx} & f_{xy} & f_{xz} \\ f_{yx} & f_{yy} & f_{yz} \\ f_{zx} & f_{zy} & f_{zz} \end{bmatrix}$$

The coefficients f_{ij} quantify the resistance force generated in direction i due to a velocity component in direction j. The tensor structure is dictated by the geometry of the porous medium. For the perforated mesh investigated in this study, the behaviour is inherently orthotropic and aligned with the principal axes. Thus, the tensor is dominated by its diagonal terms (f_{xx}, f_{yy}, f_{zz}), which couple each velocity component to its respective resistance force. Off-diagonal terms are neglected as the present geometry does not induce significant "aerodynamic lift" (i.e., a force perpendicular to the local velocity vector), unlike tilted louvre systems, which would require a full matrix representation to capture directional steering.

Due to the axial symmetry of the perforations, the transverse components are assumed to be equal ($f_{yy} = f_{zz}$), while their magnitude relative to the streamwise component (f_{xx}) depends on the mesh thickness and the openings' geometry [18].

From a numerical perspective, the D–F model prescribes a distributed momentum loss. To ensure a physically consistent pressure drop across the thickness t, the computational mesh must provide sufficient resolution within the porous volume; consistent with literature findings, a minimum of 3–5 cells across the thickness is maintained to prevent numerical instabilities and ensure grid independence of the pressure jump [4,20].

Independently of the porous medium geometrical characteristics, these coefficients can be directly derived from either experimental of numerical tests according to the procedure proposed by [18,24].

5. Results and Discussion

This section presents the results following a multi-scale validation framework, moving from the porous element scale to the building scale.

5.1. Modulus Configuration — Aerodynamic Characterisation of Porous Medium and Derivation of D–F Coefficients

This section presents the results of the identification procedure used to determine the Forchheimer resistance coefficients. The optimization procedure, taken from [18] and briefly described in Appendix A, performed for a reference thickness $t = 0.1D$, yielded

$$f_{xx} = 75.5\,\mathrm{m}^{-1}, \quad f_{yy} = f_{zz} = 2.9\,\mathrm{m}^{-1} \tag{7}$$

The high ratio between f_{xx} and f_{yy} reflects the strong directionality of the resistance, primarily concentrated in the direction normal to the screen plane.

To assess the fidelity of the homogenised model, a comparative analysis is presented in Figure 5. The force coefficients from the fully resolved simulations (explicit geometry, circle markers) are plotted against the results of the implicit simulations (Darcy–Forchheimer model, diamond markers).

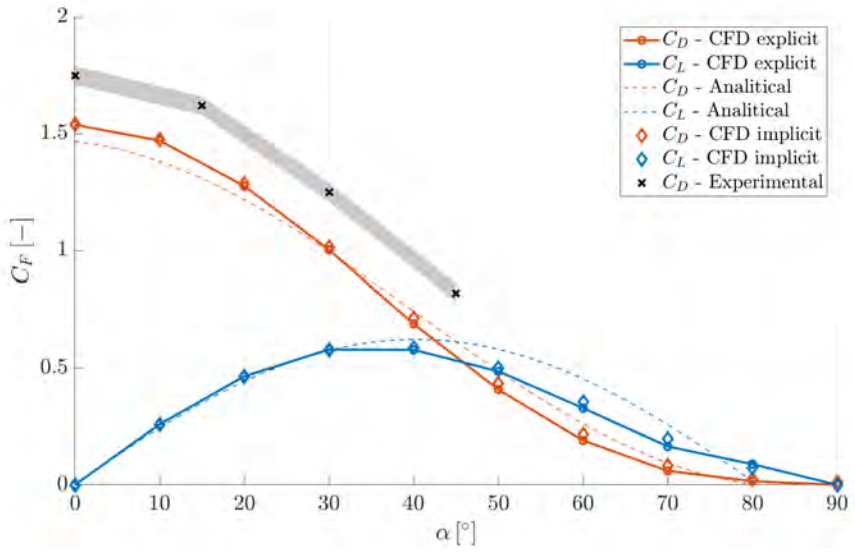

Figure 5. Porous medium characterisation. Drag (orange) and lift (blue) coefficients derived from explicit modulus simulations (circle markers), analytical model from ref. [18] (dashed lines), implicit modulus simulations (diamond markers), and experimental characterisation (black crossed markers, from ref. [25]).

The agreement between analytical and numerical approaches is excellent, with a maximum deviation below 0.5% across the full range of attack angles. This confirms that the identified coefficients perfectly capture the directional aerodynamic resistance within

the CFD environment. Furthermore, results are cross-validated against experimental drag data from Catania et al. [25] (black crosses). The procedure accurately reproduces the variation of the drag coefficient with the attack angle, with an absolute discrepancy of approximately 5.5%, likely due to inherent differences between idealised periodic boundary conditions and experimental installation effects.

Figure 6 compares the pressure field (C_p) and velocity streamlines between explicit (top) and implicit (bottom) simulations for $\alpha = 30°$ on the middle plane. The homogenized model accurately reproduces the upstream conditions and macroscopic pressure recovery downstream. However, localized discrepancies exist in the immediate near-wake ($x < 3D_H$), where the explicit geometry shows complex recirculation bubbles and streamline deviations from individual perforations.

While the implicit model cannot capture these microscopic features, previous studies show that these effects vanish as distance increases, with negligible impact on the global pressure field . In the building-scale setup, the gap is $d = 0.125D \approx 1.2D_H$. Although this is within the near-wake region, the homogenised approach's goal is to capture the overall momentum sink and pressure redistribution rather than small-scale local phenomena. This aspect is further clarified in the second part of the study, where the porous region is coupled with the solid façade and the resulting flow behaviour within the cavity between the two layers is analysed.

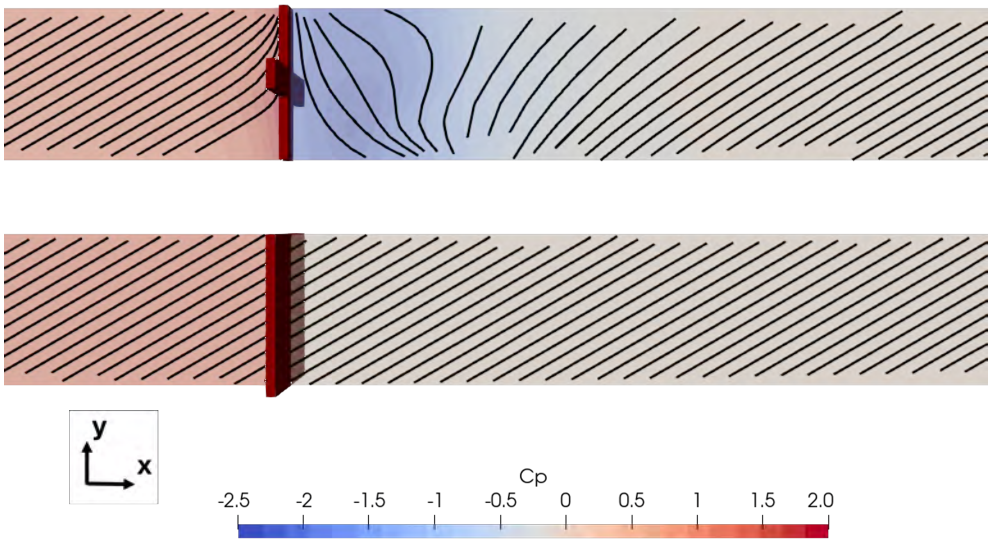

Figure 6. Modulus simulations, explicit geometry (up) and implicit porous slab (down), mean pressure coefficient (C_p) and streamlines from mean velocity field on the middle-plane, $\alpha = 30°$.

5.2. Preliminary Validation of the Building Sectional Model

To ensure the reliability of the numerical framework, the 2D sectional simulations are first validated against established literature data for a naked square cylinder. The configuration with an incidence angle of $\alpha = 0°$ is selected as the benchmark, given the extensive availability of experimental and numerical studies for this case.

Table 6 summarizes the aerodynamic parameters obtained in the current study alongside reference values from different sources. The comparison includes Strouhal number, mean drag coefficient, and standard deviation of the lift coefficient. Overall, the metrics fall well within the range of established experimental and numerical studies for sectional models, confirming the effectiveness of the current URANS setup in capturing the global aerodynamic features of the square cylinder.

This correspondence is further confirmed by the local mean pressure coefficient distribution ($C_{p,m}$), as shown in Figure 7. The numerical results (grey lines) exhibit a high degree

of agreement with experimental data (red line, from ref. [38]), with only a minor deviation observed near the trailing edges, a result consistent with the variations in drag coefficients reported in the cited literature.

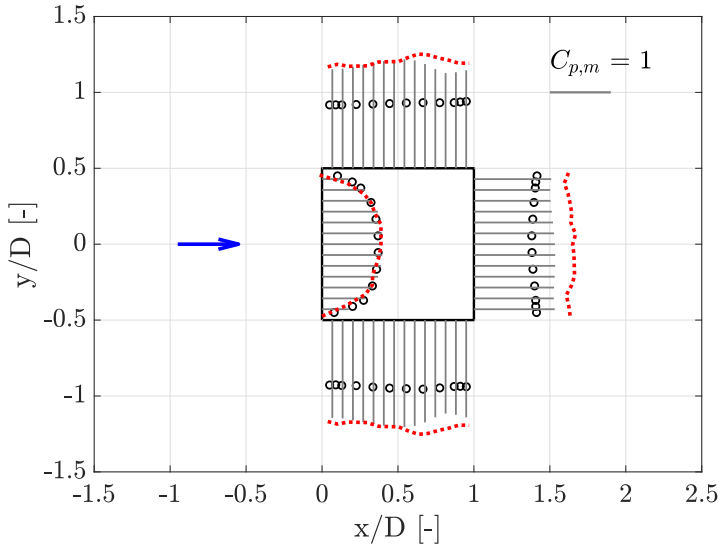

Figure 7. Wind from $\alpha = 0°$, mean pressure coefficient ($C_{p,m}$): grey bars represent 2D sectional CFD simulations, black dots denote experimental data, and red points represent literature data ref. [38]. The arrow indicates the wind direction.

However, a comparison between the 2D CFD results and the 3D experimental data (black dots, conducted on the tower configuration described in Section 3) reveals some discrepancies that can be ascribed to the different setups. As extensively discussed in the literature [26,27], the aerodynamic properties of a square cylinder shift when three-dimensional end effects are present. In 3D configurations, tip vortices and the downwash from the free end reduce the wake size, leading to lower total drag, a decrease in vortex-shedding frequency (St), and a mitigation of suction peaks on the lateral façades. These macroscopic differences are consistent with the expected flow behaviour: 2D simulations do not account for the vertical flow components and pressure equalisation typical of finite-length cylinders.

Such differences can be qualitatively appreciated from Figure 8 where a snapshot of the 2D naked simulation is compared with a smoke visualisation from the experimental tests. Despite the vortex generation following the same pattern—further confirming that the comparison is still consistent, it seems that the experimental wavelength is slightly shorter than the CFD one, likely due to the interaction with the downwash effect not explicitly reproduced in the numerical simulations.

While acknowledging these discrepancies, it should be noted that the scope of this study is not a high-fidelity replication of a specific 3D experimental setup, but rather the validation of the omogenised methodology in predicting the relative aerodynamic modifications induced by a porous envelope.

Consequently, to isolate the effect of the porous screen from the intrinsic 2D/3D modelling differences, the results are presented as a comparative study. By analysing the relative variations between the "porous" and "naked" configurations within each respective setup (2D sectional CFD and Experimental), we can evaluate the transferability and predictive capability of the D–F model independently of the absolute values.

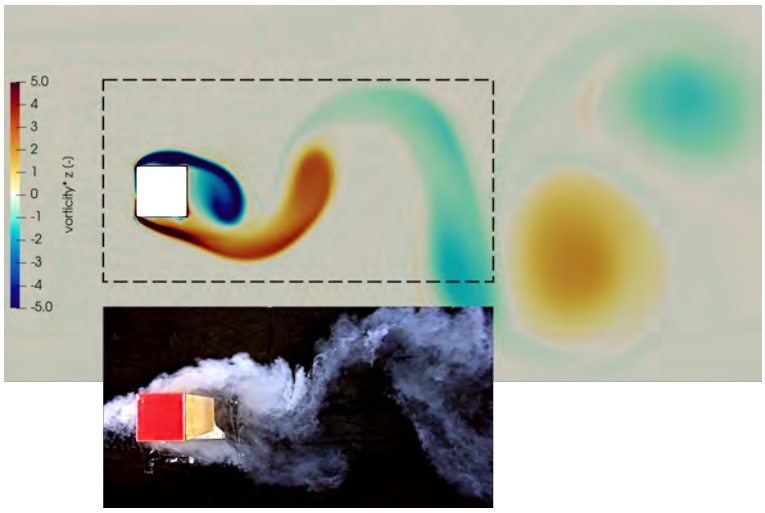

Figure 8. Comparison between a snapshot of the 2D sectional naked simulation (non-dimensional spanwise vorticity field $\omega_z^* = \omega_z D/U$) and a smoke visualization of the vortices formed in the experimental tests.

Table 6. Aerodynamic characteristics of flow over a square cylinder obtained by experiments.

Reference	TI (%)	Re/10^3	St	$C_{D,m}$	$std(C_D)$	$std(C_L)$
[39] (2D-exp)	smooth	100	0.118	–	–	1.33
[40] (2D-exp)	0.2	68.9	0.131	2.164	0.207	1.18
[41] (2D-exp)	0.5	176	0.122	2.06	–	–
[42] (2D-exp)	0.7	45.8	0.135	2.084	–	1.1
[43] (2D-exp)	0.5	47	0.128	2.15	0.27	1.18
[44] (2D-URANS)	smooth	21.4	0.137	2.07	1.37	0.06
[44] (2D-IDDES)	smooth	21.4	0.128	2.02	1.18	0.189
[38] (2D-exp)	0.5	120	0.125	2.25	–	1.40
[45] (2D-LES)	smooth	21.4	0.141	2.10	–	–
[27] (3D-LES)	smooth	12	0.104	1.62	0.07	0.15
[27] (3D-exp)	smooth	12	0.104	1.54	–	–
current study (3D-exp)	2	100	0.100	1.73	0.07	0.15
current study (2D-CFD)	smooth	67	0.123	2.05	0.02	1.48

5.3. Sectional Model — Porous Layer Effect on Local and Global Aerodynamics

Table 7 reports the primary aerodynamic properties for both the simulated and tested configurations, with wind at $\alpha = 0°$. The presence of the porous envelope is observed to drastically reduce the intensity of the fluid–structure interaction considering both mean and fluctuating load components.

The first, expressed through mean drag coefficient ($C_{D,m}$), is reduced by approximately 30% switching from naked to porous configuration. This variation is consistent with previous studies on different geometries [24,34] and confirms the significant shielding effect provided by the porous envelope. Even more pronounced is the impact on the fluctuating aerodynamic forces: a reduction of ≈80% in the standard deviation of the lift coefficient ($std(C_L)$) is consistently observed in both experimental and CFD results. This sharp decrease, also documented in other experimental works such as [46], suggests the potential of employing permeable covers to mitigate periodic vortex-shedding excitation and, as demonstrated in [3], to suppress aeroelastic phenomena such as vortex-induced vibrations.

Regarding the vortex-shedding frequency, no significant variations are observed in the configurations equipped with the porous envelope. The Strouhal number remains within 10% of the naked case, which is within the typical variability range for prisms of

this aspect ratio. While [34] observed a shift in St for a rectangular cylinder with an aspect ratio of $B/D = 3.33$ due to the effective change in geometry induced by the shroud, such a modification is not observed in the present study. This is likely because the unit aspect ratio of the square cylinder remains unchanged by the addition of the concentric porous cover.

The local pressure peaks are also effectively damped. A reduction of ≈40% in the absolute value of the suction peaks on the cross-wind faces ($-C_{p,min}$) is measured in the 2D-CFD simulations, showing excellent agreement with the experimental counterpart. Figures 7 and 9 compare the mean C_p obtained from the simulations (bars) against experimental results (circles). Despite the fact that 2D sectional CFD simulations inherently estimate higher suction levels compared to the 3D experimental setup, the overall trends and distributions remain highly consistent.

Table 7. Aerodynamic characteristics of flow over a square cylinder at $\alpha = 0°$, comparison between experimental and CFD results.

Reference	St	$-C_{p,min}$	$C_{D,m}$	$std(C_L)$
Naked 3D-exp	0.100	1.13	1.73	0.15
Porous 3D-exp	0.107	0.68	1.14	0.02
Naked 2D-exp [38]	0.125	1.80	2.25	1.40
Naked 2D-CFD	0.123	1.78	2.05	1.48
Porous 2D-CFD	0.122	1.00	1.50	0.29

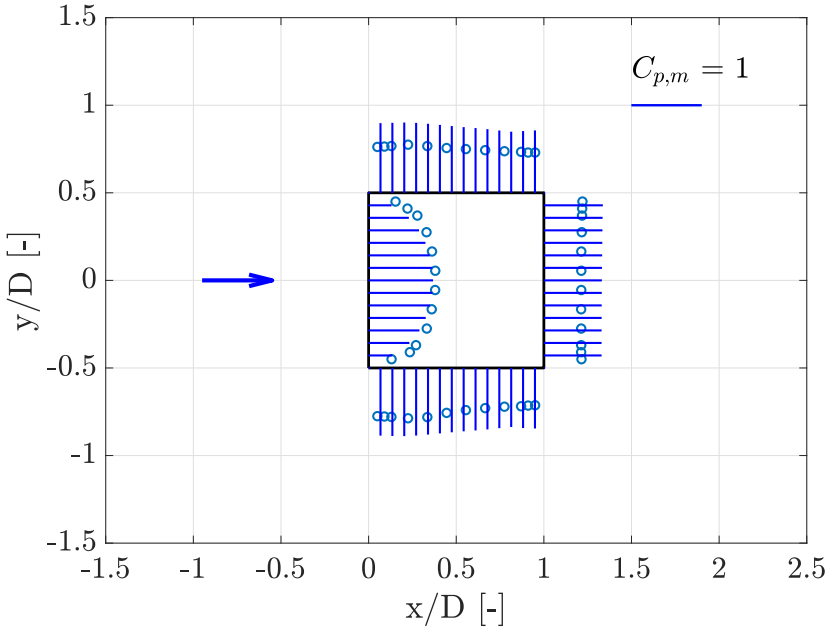

Figure 9. Wind from $\alpha = 0°$, mean pressure coefficient ($C_{p,m}$): markers represent experimental data and bars denote numerical results.

5.4. Sectional Model — Flow Physics and Wake Topology

To identify the modifications induced by the presence of the porous layer, mean pressure and velocity fields, for naked and porous configurations, are presented in Figure 10a and 10b, respectively.

The results show that the porous envelope acts as a filter, significantly modifying the pressure field, reducing both the lift fluctuations (as already shown in Table 7) on the solid façades and the suction intensity downstream of the leading edges. A new separation point at the edges of the porous envelope is created, leading to a new low-pressure region that effectively elongates and stretches the wake, shifting its recirculation centre further

downstream. This wake elongation is a primary factor in the observed reduction in the total drag coefficient.

Furthermore, the flow within the cavity (gap-flow between the solid and porous layer) contributes to a homogenization of the pressure distribution on the cross-wind faces. The normalized along-wind velocity field (u_x/U) in the porous configuration reveals a more coherent and slower recirculation zone compared to the naked case. This phenomenon is driven by the interaction between the flow separating from the envelope edges and the air circulating in the cavity between the two skins.

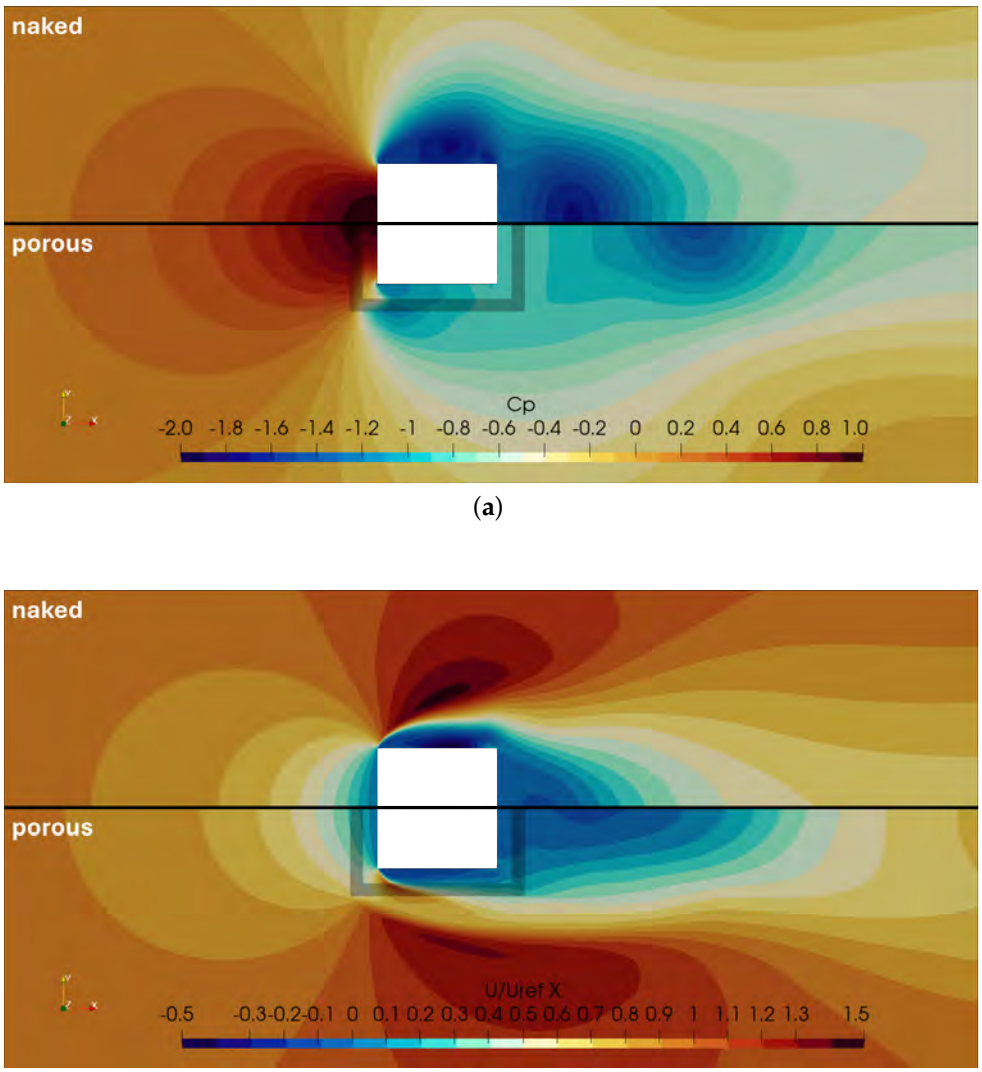

Figure 10. Sectional simulations: comparison between naked and porous configurations at $\alpha = 0°$: (**a**) mean pressure coefficient (C_p) distribution; (**b**) normalized mean wind velocity in the along-wind direction (u_x/U).

5.5. Sensitivity to Angle of Attack

To extend the analysis, the aerodynamic response is evaluated for additional wind angles of attack ($\alpha = 15°, 30°$, and $45°$). Figure 11 illustrates the ratios of the Strouhal number, mean drag coefficient, and standard deviation of the lift coefficient, between the porous and naked configurations. These plots compare numerical (2D sectional CFD) and experimental (WTT) results to quantify the contribution of the porous envelope across different orientations.

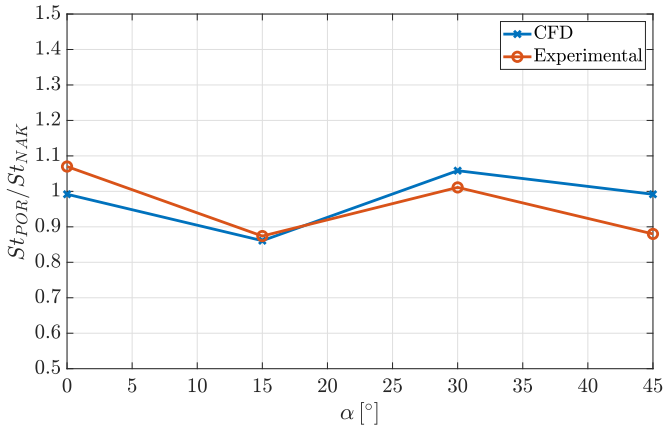

(a)

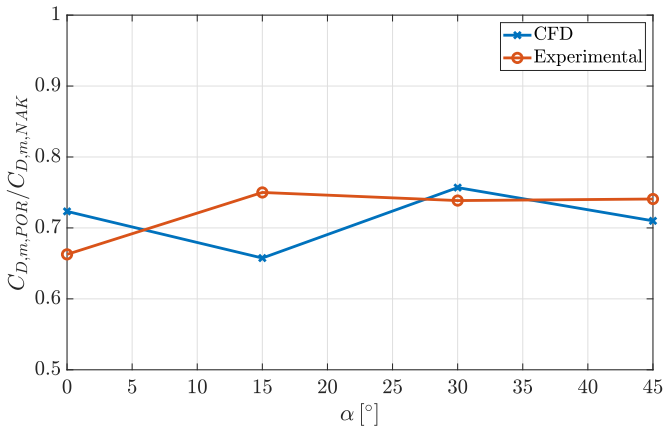

(b)

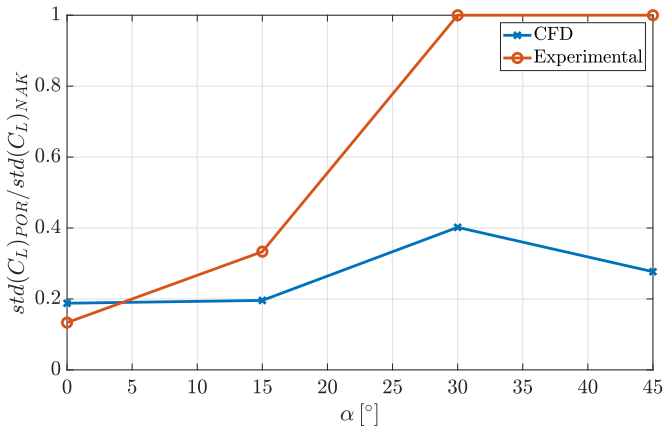

(c)

Figure 11. Aerodynamic property ratios (porous configuration against naked configuration) as a function of the angle of attack (α): (**a**) Strouhal number ratios; (**b**) mean drag coefficient ratios; (**c**) standard deviation of the lift coefficient ratios. Blue crosses denote 2D-CFD simulations and orange circles represent experimental results.

The consistency between experimental and CFD results observed for the $\alpha = 0°$ case is largely confirmed at higher angles of attack. The vortex-shedding frequency in the porous configuration remains close to that of the naked case, with a maximum reduction

of approximately 14% observed at $\alpha = 15°$ (Figure 11a). The CFD simulations accurately capture this experimental trend.

The mean drag coefficient reduction remains consistent, ranging between 25% and 35% for all tested angles (Figure 11b). For the square-cylinder geometry, this confirms the omnidirectional mitigation effect provided by the porous envelope. Again, numerical results show high consistency with the experimental counterparts.

Regarding the lift coefficient fluctuations (Figure 11c), the CFD simulations predict a reduction oscillating between 80% (for $\alpha = 0°, 15°$) and 60% (for $\alpha = 30°$). Conversely, the wind tunnel tests show negligible variations at higher attack angles. To understand this difference, note that, when $\alpha > 15°$, for the naked case, fluctuations of the lift coefficient drop to 0.02 (compared to 0.15 at $\alpha = 0°$, as reported in Table 7), mainly due to the loss of spanwise coherence and the influence of the tip vortices, as already observed by [26]. When adding the porous layer, the entity of the lift fluctuations remains unchanged (leading to $std(C_L)_{POR}/std(C_L)_{NAK}$ equal to 1), since the 3D effects keep dominating the fluid-structure interaction. Conversely, the CFD sectional model assumes perfect spatial coherence along the span, allowing for a more pronounced, albeit idealized, representation of the porous layer's mitigation effect.

The mean pressure coefficient distributions for all tested angles and configurations are compared in Figure 12. The numerical results (bars) are superimposed on the experimental data (circles) to highlight both similarities and discrepancies. As observed at $\alpha = 0°$, the primary differences occur in the separated flow regions, specifically on the leeward and cross-wind faces. In the 2D CFD setup, the flow is, by hypothesis, fully coherent in the spanwise direction, resulting in higher pressure deficits compared to the 3D experimental case.

As shown in Figure 12a,b ($\alpha = 15°$), the simulations correctly describe the overall shape of the pressure distribution and the general aerodynamic behaviour. However, the 2D model inherently predicts higher suction levels, leading to a consistent bias in both the naked and porous configurations [26,27]. Furthermore, for $\alpha > 0°$, the experimental distributions appear flatter with reduced variations along the leeward edges, possibly due to interaction with the downwash vortex from the structure's free end. These 3D effects account for the differences in absolute values between the two methods.

Nevertheless, it is noteworthy that the pressure distribution on the windward faces is captured with high accuracy in both configurations, even at high angles of attack. This is because the upwind regions are less sensitive to end effects and experimental setup variations. Even in yawed conditions involving local separation and reattachment, the model correctly describes the underlying phenomenology. This is evident at $\alpha = 30°$ (Figure 12c,d), where CFD and experimental $C_{p,m}$ distributions align, highlighting the capability of the D–F model to capture the filtering effect of the porous layer. Similar accuracy is observed at $\alpha = 45°$ (Figure 12e,f), where the symmetric distributions are faithfully reproduced, effectively capturing the windward faces' features.

In conclusion, despite the inherent limitations of 2D modelling, the results demonstrate that the overall aerodynamics and the variations induced by the porous envelope can be effectively described using the proposed homogenised approach. The Darcy–Forchheimer model, parametrised with coefficients derived from the introduced methodology, proves to be a robust and efficient tool for simulating complex façade configurations relevant for wind engineering applications. It is important to note that the identification procedure for the D–F coefficients is independent of the dimensionality of the building-scale model. The 2D assumption is therefore limited to the validation step, while the methodology itself is fully applicable to three-dimensional configurations.

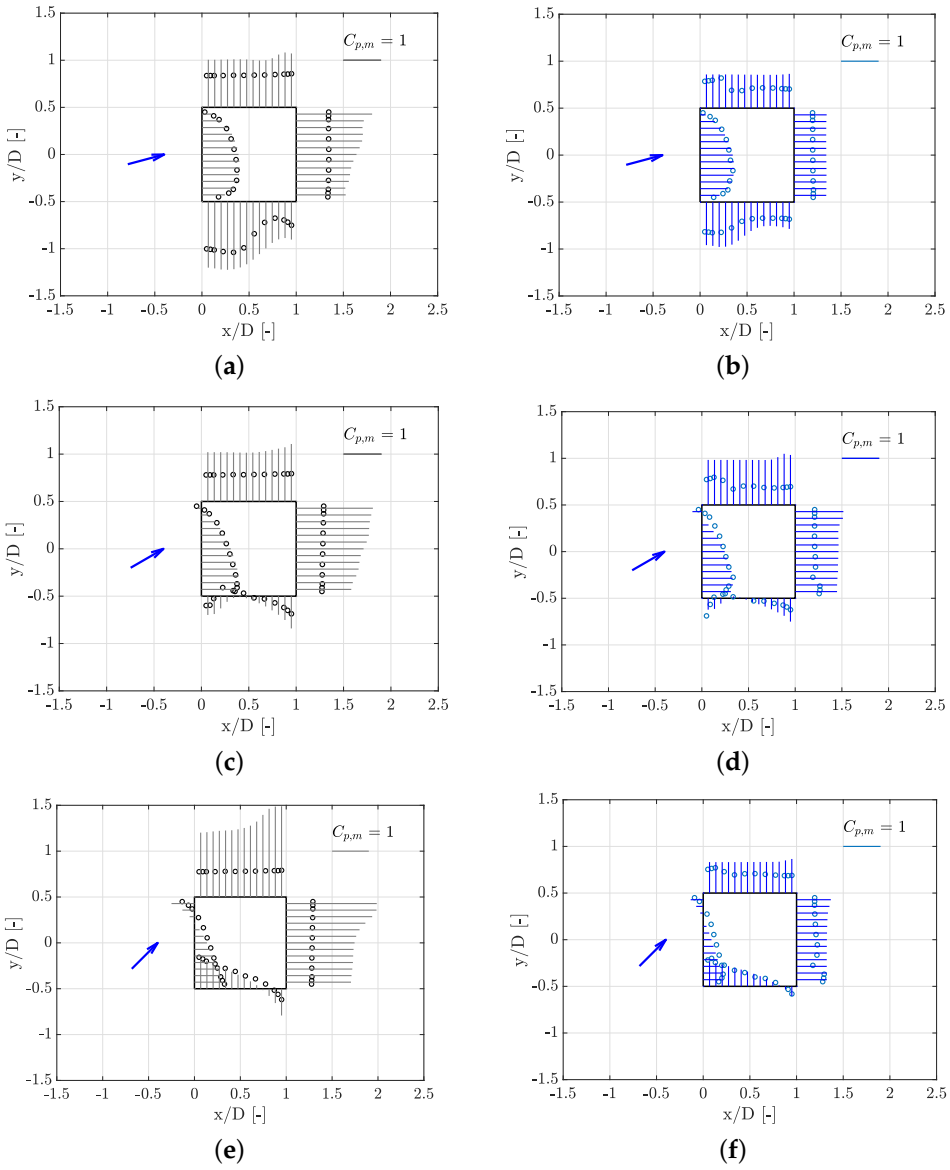

Figure 12. Mean pressure coefficient C_{pm} for different angles of attack α: (**a**) naked configuration at $\alpha = 15°$; (**b**) porous configuration at $\alpha = 15°$; (**c**) naked configuration at $\alpha = 30°$; (**d**) porous configuration at $\alpha = 30°$; (**e**) naked configuration at $\alpha = 45°$; (**f**) porous configuration at $\alpha = 45°$. Markers represent experimental data and bars denote numerical results.

6. Conclusions

This study presented a comprehensive multi-scale framework for the aerodynamic characterisation and modelling of porous envelopes in building applications. By linking high-fidelity explicit simulations at the modulus scale with homogenised D–F representations at the building scale, this work provides a validated CFD-based workflow to investigate fluid–structure interaction in permeable double-skin façades.

The main findings and conclusions of this work are summarised as follows:

- The identification procedure for the Forchheimer resistance tensor proved highly accurate. The homogenised representation reproduced the aerodynamic forces of the explicit geometry with a deviation of less than 0.5% at the modulus level and showed a robust agreement (5.5% error) with experimental data.
- The application of the validated D–F model to a square cylinder demonstrated its applicability to the case of permeable double-skin configurations by providing a fair

comparison with experimental and literature data. Despite the inherent differences in absolute suction levels between 2D URANS and 3D experimental setups due to end effects, the model successfully captured the modifications induced by the porous layer and sensitivity to the angle of attack, confirming its validity as a comparative predictive tool.

- Following the validation of the proposed methodology, the D–F model is employed to characterise the aerodynamic influence of a porous envelope on a square cylinder, representative of a simplified building configuration. At $\alpha = 0°$, a reduction of approximately 30% in the mean drag coefficient and a significant 80% reduction in lift fluctuations are observed; these trends remain consistent across higher angles of attack. The reduction in fluctuating loads, in particular, suggests a potential beneficial effect in the mitigation of aeroelastic phenomena such as vortex-induced vibrations. The simulations also reveal a clear modification of the wake topology, with the porous medium elongating the recirculation region and shifting the wake centre downstream, resulting in a reduction of suction on the structure.

Beyond the specific application presented in this study, the developed workflow provides a computationally efficient and effective engineering tool for the design of PDSF systems. The results obtained here support its applicability and motivate further investigations on more complex configurations. Future research may extend the approach to more intricate porous geometries, such as louvres or non-planar surfaces, which would require a full tensorial formulation of the D–F model. These porous media are typically characterised by strong anisotropy, leading to flow deflection effects even under a null wind attack angle. Accurately capturing this behaviour requires the inclusion of off-diagonal tensor components, coupling velocity components and forces in different directions. The proposed workflow can be naturally extended to identify such terms. Additionally, future studies should address full-building configurations in order to explicitly account for three-dimensional effects that are not captured in the present sectional approach.

Author Contributions: Conceptualization, M.C. and G.P.; methodology, M.C. and G.P.; software, M.C.; validation, M.C. and G.P.; formal analysis, M.C. and G.P.; investigation, M.C. and G.P.; resources, P.S. and A.Z.; data curation, M.C.; writing—original draft preparation, M.C.; writing—review and editing, M.C. and G.P.; visualization, M.C. ; supervision, G.P. and A.Z.; project administration, P.S.; funding acquisition, P.S. and A.Z. All authors have read and agreed to the published version of the manuscript.

Funding: This work was partially supported by the Italian Ministry of University and Research (MUR) within the framework of the PRIN 2022 project "SaFEx" (Prot. 2022F5M4HF, CUP D53C24004030006), which provided the experimental data used for the validation of the proposed methodology.

Data Availability Statement: Dataset available on request from the authors.

Acknowledgments: The authors wish to thank Luca Patruno and Claudio Somaschini for their support in providing the experimental datasets for validation purposes.

Conflicts of Interest: The authors declare no conflicts of interest.

Abbreviations

The following abbreviations are used in this manuscript:

WTT	Wind Tunnel Tests
CFD	Computational Fluid Dynamic
URANS	Unsteady Reynolds Navier–Stokes Equations
D–F	Darcy–Forchheimer

Appendix A. Analytical Computation of the D–F Coefficients

In this section, the analytical formulation of the fluid-structure forces derived by [18] and used in this study to identify the D–F coefficients is briefly reported. The control volume (CV) considered is the one described in Section 4.1.

In the case of a 2D flow through the porous screen in x-y plane, the wind speed vertical component can be considered null ($u_z = 0$), thus the momentum equation can be simplified as

$$\begin{cases} \frac{\partial p}{\partial x} = \frac{1}{2}\rho|\mathbf{u}|(f_{xx}u_x + f_{xy}u_y) \\ \frac{\partial u_y}{\partial x}u_x = -\frac{1}{2}|\mathbf{u}|(f_{yx}u_x + f_{yy}u_y) \end{cases} \tag{A1}$$

The analytical solution for u_y, decoupled from the rest of the system, allows us to derive an explicit solution for p.

$$u_y(x) = u_x \frac{2f_{yy}c_1e^{\alpha x} - f_{yx}e^{2\alpha x} + f_{yx}c_1^2}{2f_{yx}c_1e^{\alpha x} + f_{yy}e^{2\alpha x} - f_{yy}c_1^2} \tag{A2}$$

$$p(x) = c_2 - \rho\frac{f_{xx}}{f_{yy}}u_x^2 f_1(x) + 2\rho\frac{f_{xy}}{f_{yy}^2}u_x^2 f_2(x) \tag{A3}$$

defining

$\alpha = \frac{1}{2}\sqrt{f_{yy}^2 + f_{yx}^2}$, $\beta = 2f_{yx}c_1e^{\alpha x} + f_{yy}e^{2\alpha x} - f_{yy}c_1^2$;
$f_1(x) = \alpha x - \ln\beta + \ln 2$, $f_2(x) = \frac{1}{2}f_{yx}f_1 - 4c_1e^{\alpha x}\alpha^2/\beta$;
c_1, c_2 integration constants obtained by imposing proper boundary conditions.

The analytical solutions of the pressure and flow fields derived above are exact, given the inviscid, incompressible, and steady-state assumption. Thus, a CFD finite-volume solver employing a porous medium though a Forchheimer sink term is expected to provide the same results. Therefore, these solutions create a link between the Forchheimer coefficients and the macroscopic behaviour of the porous model.

Total porous forces (equivalently the forces experienced by a portion of a permeable screen) F_{Screen} can be obtained using a control volume:

$$F_{CV} = F_{Body} + F_{Screen} + F_{Pressure} + F_{Viscous} = \frac{d}{dt}\oint_{CV}\rho\, dV + \oint_{CS}\rho\mathbf{u}(\mathbf{u}\cdot\hat{n})\, dA \tag{A4}$$

where:

F_{Body} is computed integrating forces acting throughout CV such as gravity;
$F_{Pressure} = -\oint_{CS} p\,\hat{n}\, dA$;
$F_{Viscous}$ is computed integrating the viscous stresses on the Control Surface (CS).

Disregarding gravitational and viscous forces in an incompressible steady flow, total porous resistance can be computed:

$$F_{Screen} = \oint_{CS}\rho\mathbf{u}(\mathbf{u}\cdot\hat{n})\, dA + \oint_{CS} p\,\hat{n}\, dA \tag{A5}$$

In the specific case of a cyclic domain:

$$\begin{cases} F_x = (p|_{x=0} - p|_{x=t})(h_H \cdot b_H) \\ F_y = \rho u_x(u_y|_{x=0} - u_y|_{x=t})(h_H \cdot b_H) \\ F_z = \rho u_x(u_z|_{x=0} - u_z|_{x=t})(h_H \cdot b_H) \end{cases} \tag{A6}$$

where h_H, b_H, and t are the control volume dimensions for the permeable screen/equivalent porous media considered. For more information of the model derivation, please refer to ref. [18].

References

1. Zasso, A.; Perotti, F.; Rosa, L.; Schito, P.; Pomaranzi, G.; Daniotti, N. Wind pressure distribution on a porous double skin facade system. In *Proceedings of the XV Conference of the Italian Association for Wind Engineering*; Springer: Cham, Switzerland, 2019; pp. 730–741. https://doi.org/10.1007/978-3-030-12815-9_55.
2. Teimourian, A.; Teimourian, H. Vortex Shedding Suppression: A Review on Modified Bluff Bodies. *Eng* **2021**, *2*, 325–339.
3. Catania, M.; Pomaranzi, G.; Zasso, A. The role of Permeable Double Skin Façades on the onset of VIV on high-rise buildings. *J. Wind Eng. Ind. Aerodyn.* **2024**, *253*, 105831.
4. Catania, M.; Pomaranzi, G.; Fontanella, A.; Zasso, A. Modelling of Wind Turbines as Porous Disks for Wind Farm Flow Studies. *J. Phys. Conf. Ser.* **2024**, *2767*, 052049.
5. Alvarez, A.J.; Nieto, F.; Nguyen, D.T.; Owen, J.S.; Hernandez, S. 3D LES simulations of a static and vertically free-to-oscillate 4:1 rectangular cylinder: Effects of the grid resolution. *J. Wind Eng. Ind. Aerodyn.* **2019**, *192*, 31–44.
6. Bruno, L.; Fransos, D.; Coste, N.; Bosco, A. 3D flow around a rectangular cylinder: A computational study. *J. Wind Eng. Ind. Aerodyn.* **2010**, *98*, 263–276.
7. Bruno, L.; Salvetti, M.V.; Ricciardelli, F. Benchmark on the Aerodynamics of a Rectangular 5:1 Cylinder: An overview after the first four years of activity. *J. Wind Eng. Ind. Aerodyn.* **2014**, *126*, 87–106. https://doi.org/10.1016/j.jweia.2014.01.005.
8. Marchand, O.C.; Ramananarivo, S.; Duprat, C.; Josserand, C. Three-dimensional flow around and through a porous screen. *J. Fluid Mech.* **2024**, *987*, A20.
9. Shen, G.; Bao, X.; Yao, J.; Yu, S. Experimental investigation on wind loads of planar porous façades. *J. Build. Eng.* **2025**, *103*, 112199.
10. Azizi, F. On the pressure drop of fluids through woven screen meshes. *Chem. Eng. Sci.* **2019**, *207*, 464–478.
11. Tominaga, Y.; Shirzadi, M. RANS CFD modeling of the flow around a thin windbreak fence with various porosities: Validation using wind tunnel measurements. *J. Wind Eng. Ind. Aerodyn.* **2022**, *230*, 105176. https://doi.org/10.1016/j.jweia.2022.105176.
12. Feichtner, A.; Mackay, E.; Tabor, G.; Thies, P.R.; Johanning, L. Comparison of Macro-Scale Porosity Implementations for CFD Modelling of Wave Interaction with Thin Porous Structures. *J. Mar. Sci. Eng.* **2021**, *9*, 150.
13. Xu, M.; Patruno, L.; de Miranda, S. A pressure–velocity jump approach for the CFD modelling of permeable surfaces. *J. Wind Eng. Ind. Aerodyn.* **2023**, *233*, 105317.
14. Xu, M.; Patruno, L.; Lo, Y.L.; de Miranda, S. Simulation strategies for wind shields and porous barriers for bridge deck optimization. *Structures* **2022**, *40*, 824–839.
15. Darcy, H. *Les Fontaines Pubbliche de la Ville de Dijon*; Victor Dalmont: Paris, France, 1856.
16. Forchheimer, P. Wasserbewegung durch Boden. *Z. Ver. Dtsch. Ing.* **1901**, *45*, 1781–1788.
17. Chen, H.; Christensen, E.D. Investigations on the porous resistance coefficients for fishing net structures. *J. Fluids Struct.* **2016**, *65*, 76–107.
18. Marykovskiy, Y.; Pomaranzi, G.; Schito, P.; Zasso, A. A Method to Evaluate Forchheimer Resistance Coefficients for Permeable Screens and Air Louvers Modelled as a Porous Medium. *Fluids* **2024**, *9*, 147.
19. Cao, J.; Gao, H.; Dou, L.; Zhang, M.; Li, T. Modeling flow in anisotropic porous medium with full permeability tensor. *J. Phys. Conf. Ser.* **2019**, *1324*, 012054.
20. Pomaranzi, G.; Bistoni, O.; Schito, P.; Rosa, L.; Zasso, A. Wind Effects on a Permeable Double Skin Façade, the ENI Head Office Case Study. *Fluids* **2021**, *6*, 415. https://doi.org/10.3390/fluids6110415.
21. Ooi, C.; Chiu, P.H.; Raghavan, V.; Wan, S.; Poh, H.J. Porous media representation of louvers in building simulations for natural ventilation. *J. Build. Perform. Simul.* **2019**, *12*, 494–503.
22. Raffaele, L.; Coste, N. CWE study of the aerodynamic interaction between a porous fence and a ground-mounted solid obstacle via pressure jump approach. *J. Wind Eng. Ind. Aerodyn.* **2025**, *266*, 106198. https://doi.org/10.1016/j.jweia.2025.106198.
23. Xu, M.; Patruno, L.; Lo, Y.L.; de Miranda, S. On the use of the pressure jump approach for the simulation of separated external flows around porous structures: A forward facing step. *J. Wind Eng. Ind. Aerodyn.* **2020**, *207*, 104377.
24. Pomaranzi, G.; Bistoni, O.; Schito, P.; Zasso, A. Numerical modelling of three-dimensional screens, treated as porous media. *Wind Struct.* **2021**, *33*, 409–422.
25. Catania, M.; Giacomoni, F.; Pomaranzi, G.; Schito, P.; Zasso, A.; Somaschini, C.; Patruno, L. A Novel Combined Experimental and Numerical Methodology for Aerodynamic Characterisation of Porous Media. *Preprints* **2026**. https://doi.org/10.20944/preprints202603.1073.v1.
26. Sakamoto, H.; Arie, M. Vortex shedding from a rectangular prism and a circular cylinder placed vertically in a turbulent boundary layer. *J. Fluid Mech.* **1983**, *126*, 147–165. https://doi.org/10.1017/S0022112083000087.

27. Rastan, M.R.; Shahbazi, H.; Sohankar, A.; Alam, M.M.; Zhou, Y. The wake of a wall-mounted rectangular cylinder: Cross-sectional aspect ratio effect. *J. Wind Eng. Ind. Aerodyn.* **2021**, *213*, 104615. https://doi.org/10.1016/j.jweia.2021.104615.
28. Versteeg, H.K.; Malalasekera, W. *An Introduction to Computational Fluid Dynamics: The Finite Volume Method*; Pearson Education Limited: Harlow, UK, 2007.
29. Shimada, K.; Ishihara, T. Application of a Modified k–ϵ Model to the Prediction of Aerodynamic Characteristics of Rectangular Cross-Section Cylinders. *J. Fluids Struct.* **2002**, *16*, 465–485.
30. Kang, Z.; Zhang, C.; Chang, R.; Ma, G. A numerical investigation of the effects of Reynolds number on vortex-induced vibration of the cylinders with different mass ratios and frequency ratios. *Int. J. Nav. Archit. Ocean Eng.* **2019**, *11*, 835–850.
31. Liu, F. A Thorough Description Of How Wall Functions Are Implemented In OpenFOAM. In *Proceedings of CFD with OpenSource Software*; Nilsson, H., Ed.; Chalmers University of Technology: Gothenburg, Sweden, 2016.
32. Allori, D.; Bartoli, G.; Mannini, C. Wind tunnel tests on macro-porous structural elements: A scaling procedure. *J. Wind Eng. Ind. Aerodyn.* **2013**, *123*, 291–299.
33. Tian, X.; Ong, M.C.; Yang, J.; Myrhaug, D. Unsteady RANS simulations of flow around rectangular cylinders with different aspect ratios. *Ocean Eng.* **2013**, *58*, 208–216.
34. Catania, M.; Pomaranzi, G.; Zasso, A. From vortex shedding to Vortex-Induced Vibrations: The role of porous façades. *J. Fluids Struct.* **2026**, *143*, 104538. https://doi.org/10.1016/j.jfluidstructs.2026.104538.
35. Leontini, J.S.; Thompson, M.C. Vortex-induced vibrations of a diamond cross-section: Sensitivity to corner sharpness. *J. Fluids Struct.* **2013**, *39*, 371–390.
36. Rocchio, B.; Mariotti, A.; Salvetti, M.V. Flow around a 5:1 rectangular cylinder: Effects of upstream-edge rounding. *J. Wind Eng. Ind. Aerodyn.* **2020**, *204*, 104237.
37. Yang, Q.; Zheng, C.; Ruan, G.; Liu, X. Aerodynamic characteristics of rounded-corner rectangular cylinders based on wind tunnel model test. *Exp. Therm. Fluid Sci.* **2025**, *169*, 111566.
38. Yang, Q.; Yu, C.; Liu, X.; Yu, W.; Jiang, H. Study on the aerodynamic characteristics and flow mechanism of square cylinders with rounded corners. *Structures* **2024**, *62*, 106298.
39. Vickery, B.J. Fluctuating lift and drag on a long cylinder of square cross-section in a smooth and in a turbulent stream. *J. Fluid Mech.* **1966**, *25*, 481–494.
40. Noda, H.; Nakayama, A. Free-stream turbulence effects on the instantaneous pressure and forces on cylinders of rectangular cross section. *Exp. Fluids* **2003**, *34*, 332–344.
41. Lee, B.E. The effect of turbulence on the surface pressure field of a square prism. *J. Fluid Mech.* **1975**, *69*, 263–282.
42. Liu, M.; Xiao, L.; Yang, L. Experimental investigation of flow characteristics around four square-cylinder arrays at subcritical Reynolds numbers. *Int. J. Nav. Archit. Ocean Eng.* **2015**, *7*, 906–919.
43. Alam, M.M.; Zhou, Y.; Wang, X.W. The wake of two side-by-side square cylinders. *J. Fluid Mech.* **2011**, *669*, 432–471.
44. Ke, J. RANS and hybrid LES/RANS simulations of flow over a square cylinder. *Adv. Aerodyn.* **2019**, *1*, 10. https://doi.org/10.1186/s42774-019-0012-9.
45. Minguez, M.; Brun, C.; Pasquetti, R.; Serre, E. Experimental and high-order LES analysis of the flow in near-wall region of a square cylinder. *Int. J. Heat Fluid Flow* **2011**, *32*, 558–566.
46. Pomaranzi, G.; Daniotti, N.; Schito, P.; Rosa, L.; Zasso, A. Experimental assessment of the effects of a porous double skin facade system on cladding loads. *J. Wind Eng. Ind. Aerodyn.* **2020**, *196*, 104019.